Materials Science & Engineering A 925 (2025) 147868

Contents lists available at ScienceDirect

Materials Science & Engineering A

journal homepage: www.elsevier.com/locate/msea

Effects of volumetric energy density on defect structure and fatigue behaviour of powder bed fusion manufactured 316L stainless steel

Matias Jaskari [a,*], Atef Hamada [a], Tarek Allam [b,c], Krzysztof Dzieciol [d], Sumit Ghosh [e], Ruth Schwaiger [b], Pentti Karjalainen [e], Antti Järvenpää [a]

[a] FMT-research Group, Kerttu Saalasti Institute, University of Oulu, Pajatie 5, 85500, Nivala, Finland
[b] Institute of Energy Materials and Devices: Microstructure and Properties of Materials (IMD-1), Research Center Jülich, 52428, Jülich, Germany
[c] Department of Metallurgical and Materials Engineering, Suez University, 43528, Suez, Egypt
[d] Institute of Energy Technologies, Fundamental Electrochemistry (IET-1), Research Center Jülich, 52428, Jülich, Germany
[e] Centre of Advanced Steels Research, University of Oulu, PO Box 4200, 90014, Finland

ARTICLE INFO

Keywords:
Laser beam powder-bed fusion
316L stainless steel
Volumetric energy density
Defects
Fatigue strength

ABSTRACT

Three structures of AISI 316L austenitic stainless steel were additively manufactured using the laser beam powder bed fusion (PBF-LB) process with varying volumetric energy density (VED) levels: low (50.8 J/mm³), medium (79.4 J/mm³), and high (84.3 J/mm³). The impact of VED on defects, microstructure, and fatigue behaviour was investigated and compared to wrought 316L steel. Various novel techniques were used to analyse the grain structure and defects. Fatigue behaviour was assessed through low and high cycle fatigue tests and tensile tests at room temperature.

Results showed that increasing VED improved material density (from 91.8 % to 99.6 %) and reduced defect size and complexity. Both lack of fusion (LoF) and pore-type defects were identified, with fewer and less complex LoF defects at higher VED. Defects were primarily located at subsurface regions corresponding to the border hatch-fill contour layer. Printed structures exhibited lower high cycle fatigue (HCF) strength than wrought steel, but this difference diminished in low cycle fatigue (LCF) regimes for medium and high VED structures, where twinning and martensitic transformation enhanced fatigue strength. The defect characteristics significantly influenced HCF strength, and achieving a fatigue limit comparable to wrought steel requires very low defect density even at high VED.

1. Introduction

Additive manufacturing (AM) has emerged as a highly effective method for producing prototypes and small-scale batches of finished products, offering opportunities to optimize materials, weight, and geometries during the design phase [1,2]. While various techniques are evolving for industrial applications, laser beam powder bed fusion (PBF-LB) remains a predominant method for AM with metallic materials [3] However, PBF-LB is a multifaceted process that necessitates meticulous consideration of numerous processing parameters and powder characteristics. In particular, the fabrication of AISI 316L austenitic stainless steel through PBF-LB presents noteworthy challenges. Factors such as powder humidity and oxygen content play pivotal roles in the outcome. Elevated oxygen levels can escalate the risk of pore formation during fabrication [4] while the size distribution of powder granules and recycling rates impact flow and densification properties [5,6].

Remarkably, the literature indicates that over 100 parameters can potentially impact the quality of the final product [7]. It is widely acknowledged that the pore and lack of fusion (LoF) defects and microstructural characteristics of AM components are markedly influenced by a critical variable known as volumetric energy density (VED). VED is a composite measure derived from five printing parameters: laser power, scanning speed, laser spot size, hatch spacing, and layer thickness [8–10]. The equation for calculating the VED is commonly shown as follows [11,12]:

$$VED = \frac{P}{v\sigma t}\left[\frac{J}{mm^3}\right], \quad (1)$$

where P, v, σ and t are the laser power, scan speed, hatch spacing, and layer thickness, respectively. Consequently, VED should be employed

* Corresponding author.
E-mail address: matias.jaskari@oulu.fi (M. Jaskari).

https://doi.org/10.1016/j.msea.2025.147868
Received 9 September 2024; Received in revised form 20 December 2024; Accepted 14 January 2025
Available online 16 January 2025

judiciously as a defining parameter, though with caution exercised in its direct application [13,14]. Nonetheless, numerous studies have examined the influence of VED on the density level and ultimate microstructure of materials produced through PBF-LB. For instance, Leicht et al. [15] observed that increasing the VED resulted in coarser grains of dendritic cellular substructure, accompanied by an increased specific density of the 3D-printed 316L steel. Cherry et al. [16] demonstrated that precise control and optimization of VED could result in an impressive physical density of 99.6 % at a high VED of 104.5 J/mm^3. Choo et al. [17] studied the effect of laser power on achievable density of printed 316L, and they reported that the density could be manipulated in an optimal VED range of 54–102 J/mm^3. Larimian et al. [18] investigated the effects of VED and scanning strategy on the density, concluding that higher VED led to denser structures, though the scanning strategy exhibited a more pronounced influence on the density. The effect of VED on the density has also been extensively examined in the context of other AM materials, such as Ti6Al4V [19], Inconel 718 [20], and AlSi10Mg [21], yielding similar conclusions.

Sanaei and Fatemi [22] have listed the major defect types commonly observed in AM metals and their sources. LoF defects, arising from insufficient energy input, and gas porosity, resulting from excessive energy, are the main types identified. These defects' characteristics, including type, location, shape, size, orientation, and density, are significantly influenced by the parameters of the manufacturing process. Gas pores typically take on a spherical or ellipsoidal shape within the material. Inadequate energy input can lead to LoF defects, where layers or laser tracks fail to bond adequately, often showing sharp edges. Therefore, while increasing energy density too much may slightly decrease the overall density of the part from the ideal, it can help mitigate LoF defects by promoting the formation of spherical pores, which can alleviate stress concentrations. This strategic adjustment underscores the delicate balance between maintaining part integrity and minimizing defects in AM processes.

The literature documents extensively the correlation between the mechanical properties of AM materials and microstructural defects, both the porosity level and defect distribution. Jost et al. [23], while examining the influence of spatial energy density on the porosity and mechanical properties, revealed that smaller defects did not have a considerable effect on static properties of PBF-LB 316L. In our prior investigation [24], a marginal impact of defects was observed on the tensile strength of PBF-LB 316L within a specific parameter range when varying the applied VED. However, an improvement in elongation was noted, increasing from 35 % to 50 % as the VED was increased from 50.8 to 84.3 J/mm^3. Consistently, Röttger et al. [25] demonstrated a correlation between elongation and achieved material density.

The few examples mentioned above suggest that VED and defect structure may not significantly impact the static mechanical properties. However, their effect becomes more pronounced in fatigue properties, prompting numerous studies on the dynamic behaviour of printed structures in the literature, e.g., a review given by Sanaei and Fatemi [22]. Ponticelli et al. [26] demonstrated that the fatigue limit (FL) of PBF-LB 316L could be as low as 20 % of the material's ultimate tensile strength in reversed bending fatigue. Moreover, it was shown that ductility plays a more important role than refining grain size on FL for PBF-LB 316L. For example, comparisons showed higher ductility for 316 steel due to more austenite phase contained in rolled 316 steel than the PBF-LB one [27].

The VED-porosity relationship in AM metallic structures serves as a comprehensive index for evaluating the fatigue behaviour of PBF-LB 316L parts [22,28–42]. However, the defect structure consists of spherical pores and sharp elongated LoF defects, having different influence. Shrestha et al. [43] delved into the fatigue performance of PBF-LB 316L in various directions through strain-controlled axial fatigue testing. Their findings revealed that the fatigue life was influenced by the relative shape of defects perpendicular to the loading direction. Kumar et al. [44] investigated the static and cyclic behaviours of 316L manufactured using two techniques: binder jet printing and PBF-LB. They observed that even though PBF-LB induced lower porosity, the achieved fatigue strength was significantly inferior. This was attributed to the presence of sharp LoF defects and a long columnar dendritic microstructure, facilitating easier crack propagation.

Several studies have reported a range of low values for FL of PBF-LB 316L. For instance, Blinn et al. [45] noted an FL of 150 MPa for the as built 316L structure. Jaskari et al. [34] observed FL as low as 100 MPa in flexural bending fatigue. Solberg et al. [33] demonstrated that in rotation bending fatigue, a high level of porosity shifts the initiation of subsurface cracks, lowering the fatigue strength of highly porous samples to 163 MPa (at 2×10^6 cycles, load ratio R = 0.1). Liang et al. [46] reported FL in the range of 80–120 MPa at 2×10^6 cycles in axial fatigue and 80–140 MPa in bending fatigue (R = −1) depending on surface condition, while the FL of wrought 316L in bending fatigue was 280 MPa. Hamada et al. [47] investigated the fatigue damage mechanism in PBF-LB 316L, both in its as-built state and after heat treatment at 900 °C for 30 min, under uniaxial load-controlled push-pull dynamic loading. Their findings highlighted that pores, dendritic cellular structures, and residual stresses are the primary factors contributing to fatigue damage in the as built 316L specimens. Consequently, the FL demonstrated a notable increase after the heat treatment, rising from 75 to 150 MPa.

However, Elangeswaran et al. [48] highlighted that by achieving the density of 99.4 % and preparing the samples by machining, the fatigue strength estimated at about 300 MPa at 2×10^6 cycles, even surpassed that of the wrought 316L. The FL of 285–310 MPa was also achieved by Jaskari et al. [49] as using specimens, machined from printed rods and electropolished after stress relieving.

As is obvious from the above brief description of the state of the art of the relationship between defect structure and fatigue properties of AM 316L steel, the impairing influence of defects has been firmly demonstrated. However, the influence of the printing parameters and particularly the influence of the VED on defect structure and consequent fatigue life is more scarcely investigated. By employing a diverse range of laser parameters, the VED levels during the PBF-LB printing process of 316L were adjusted, thereby providing different density and defect distribution profiles. The novelty of the present approach lies in the nuanced investigation of the influence of VED in PBF-LB on the achieved defect characteristics and distribution and thereby on fatigue resistance, shedding light on the capability of printed structures to withstand fatigue damage. The study goes beyond conventional analyses by employing advanced techniques such as microtomography for comprehensive characterizations of intrinsic defects. As few examples, Hastie et al. [21] classified shape of pores by X-ray micro-computed tomography in PBF-LB AlSi10Mg, while Hu et al. [50] applied synchrotron radiation X-ray topography to characterize the defect morphology and depict the defect evolution during in-situ tensile tests of an additively manufactured Ti-6Al-4V alloy, and recently Wang et al. [51] used this technique for PBF-LB IN718 superalloy to establish the relation between defect characteristics of machined samples and fatigue life. Furthermore, our present study delves into the intricate deformation mechanisms within the PBF-LB printed structures of 316L during cyclic straining, leveraging electron backscatter diffraction and transmission electron microscopy. This multi-faceted exploration not only adds valuable insights to the field of AM but also enhances the understanding of the effect of PBF-LB parameters on fatigue resistance of 316L.

2. Materials and methods

2.1. Laser powder bed fusion processing

The 316L powder utilized in the present PBF-LB deposition process was provided by SLM Solutions. The powder underwent sieving to eliminate larger particles of the order of 50 μm. The chemical composition of the 316L powder along with that of the as-built material, the former being a nominal one given by the SLM Solutions and the latter

measured by a glow discharge optical emission spectroscope (GDOES, Spectruma GDA750), are listed in Table 1.

Three sets of samples were deposited using an SLM 280HL PBF-LB equipment. By varying the scanning speed and laser power, three different VED levels, low (L-VED at 50.8 J/mm^3), medium (M-VED at 79.4 J/mm^3), and high (H-VED at 84.3 J/mm^3) were applied aiming to vary microstructural features and internal defect characteristics, such as defect number, size, shape, and distribution. The VED parameters are outlined in Table 2. The printing parameters for the border hatch and the contour fill between the fill and border hatch were kept constant, and their values are also given in Table 2.

Cylindrical fatigue specimens, featuring a total length of 55 mm and diameter of 6 mm, were vertically fabricated to their final shape. The specific sample orientations and the printing pattern strategy used are detailed in Fig. 1a and b. Notably, after the completion of each layer, schematic of the laser scanning of a layer shown in Fig. 1c, the hatching track underwent a rotation of 35°. Subsequent to the deposition, the samples underwent stress-relief annealing at 600 °C for 120 min under an argon atmosphere, followed by furnace cooling to room temperature.

2.2. Metallography

The density of the PBF-LB processed 316L steel samples was first determined using the Archimedes' method. The quantitative analysis of internal defect distribution and size was performed using a Micro-Computed Tomography (μCT) scanner (XRADIA Versa 620 laboratory μCT system). The X-ray tube was configured to operate at 140 kV, enabling penetration through relatively thick cross sections comprised of high-Z materials. To mitigate hardening effects caused by the beam, a high-pass filter was interposed between the source and the sample. The utilization of a short 2-s exposure facilitated the acquisition of a substantial number of projections (1600), resulting in high-quality tomograms. The μCT measurements encompassed the entire volume of the parallel length of a fatigue specimen, which measures 12 mm, as depicted in Fig. 1a. Used voxel size for the measurements was around 7 μm, voids smaller than 27 voxels (3 × 3 × 3) were excluded to remove noise.

The microstructures and defects on cross-sections of built L-PBF 316L steel as well as after fatigue experiments on fracture surfaces were examined using a laser confocal scanning microscope (LCSM, KEYENCE/VK-X200). For microstructural examination, the samples underwent electropolishing using a perchloric acid solution, followed by electrochemical etching in a concentrated nitric acid solution at 1.2 V. Scanning electron microscopy (SEM; JEOL JSM7900F) and electron backscatter diffraction (EBSD) examinations were conducted by the Oxford Instruments Symmetry S2 system, with an acceleration voltage of 20 kV and a working distance of 17 mm. Step size was varied according to the used magnification, being between 0.1 and 0.8 μm. Transmission and scanning transmission electron microscopy (TEM/STEM) analyses were performed utilizing a JEOL JEM2200FS microscope, with lamellae extracted from sample surfaces using the focused ion beam technique (FIB, FEI Helios DualBeam).

2.3. Measurement of mechanical properties

To evaluate the quasi-static tensile properties of the 316L materials printed with various VEDs, uniaxial tensile tests were performed at a strain rate of 0.008 s^{-1} in accordance with the standard EN-ISO 6892-1, using a Zwick Z100 testing machine equipped with an external extensometer. The round specimens (see Fig. 1b) had the following dimensions: a total length of 35 mm, a gauge length of 25 mm, and a diameter of 6 mm. The tensile tests were repeated three times for the three sets of samples.

Hardness measurements were conducted using a Zwick ZHU 2.5 hardness tester with the Vickers indenter and the load of 10 kg, and the measurement was repeated 5 times for each measured structure.

Two distinct fatigue regimes, encompassing low-cycle fatigue (LCF < 10^5 cycles) and high-cycle fatigue (HCF, 10^5–10^7 cycles), were implemented using two different testing machines. For LCF testing, a servo-hydraulic dynamic testing machine (MTS810) operated in a force-control mode at a frequency of 15 Hz. HCF tests were conducted using an electromagnetic resonator (Zwick Vibrophore) with a testing frequency of 100 Hz. All tests were executed under fully reversed loading conditions (R = −1). The fatigue limit was determined for unbroken samples at a cut-off of 10^7 cycles. During the tests, the surface temperature of the specimens was monitored using a PT100 sensor, and pressure air flow was applied to prevent specimen heating.

Before fatigue testing, the samples underwent mechanical grinding to 600 grit and subsequent electropolishing to achieve a mirror finish (average surface roughness value R_a < 0.1 μm). The grinding and polishing process was conducted to remove a minimal amount of material (approximately 100 μm) from the sample surface, ensuring that most defects remained in the material. 15 samples were tested for each set.

3. Results

3.1. As-built microstructures

The microstructural characteristics of the as built 316L steel, printed at different VEDs, are depicted in Fig. 2 in a section parallel to the building direction (BD). The observed structure with distinct melt pool boundaries is a result of the melting tracks generated by the laser beam. Fig. 2 further illustrates the impact of VED on the dimensions of the width and depth of the melt pools, the values outlined in Table 3. Average width and height were calculated using Feret's diameter, and equivalent diameter were calculated from measured melt pool area. It can be noted that the effect of VED was more pronounced between the L-VED and M-VED, showing clear coarsening both in melt pool average size as well as flattening of melt pool. The increase in VED from the medium to high level did not notably affect the melt pool size or grain size, but columnar grains were observed in the H-VED structure after etching, as is shown as red dashed lines in Fig. 2c.

The changes in the melt pool size and morphology can be simply attributed to the energy deposited into the material. In Fig. 2a and b, black defects are also seen, as outlined by yellow dashed line. They locate at melt pool boundaries and have elongated truncated shape, so that they could be classified as LoF defects.

The achieved density measured using the Archimedes' method was 91.9, 98.9 and 99.6 % for L-VED, M-VED and H-VED, respectively. Therefore, the overall defect density decreases with increasing the VED.

The crystallographic microstructure of the PBF-LB 316L steel printed at various VEDs seen in EBSD maps is depicted in Fig. 3. The IPF maps of the three structures reveal grains with irregular morphology, as seen parallel to the BD. In the case of L-VED printing, the grain structure is accompanied by a few internal defects, as shown in Fig. 3a.

With increasing the VED, the grain structure evolves into a more

Table 1
Nominal 316L powder composition for PBF-LB manufacturing and corresponding as-built material composition in wt. %.

	C	Cr	Ni	Mn	Mo	Si	Ti	Nb	N	Fe
Powder 316L	0.03	17*/19**	13*/15**	2	2.2*/3**	0.7	–	–	–	Bal.
PBF-LB 316L	0.02	17.7	12.9	0.6	2.5	0.7	0.01	0.005	0.09	Bal.

The symbols * and ** denote the minimum and maximum contents of the element, respectively.

Table 2
Fabrication parameters for 316L samples with varying VED.

ID	VED [J/mm^3]	Laser power [W]	Scanning speed [mm/s]	Hatch spacing [μm]	Layer thickness [μm]
L-VED	50.8	160	875	120	30
M-VED	79.4	190	800	100	30
H-VED	84.3	220	725	120	30
Border hatch	104.2	100	400	80	30
Fill contour	92.6	125	500	90	30

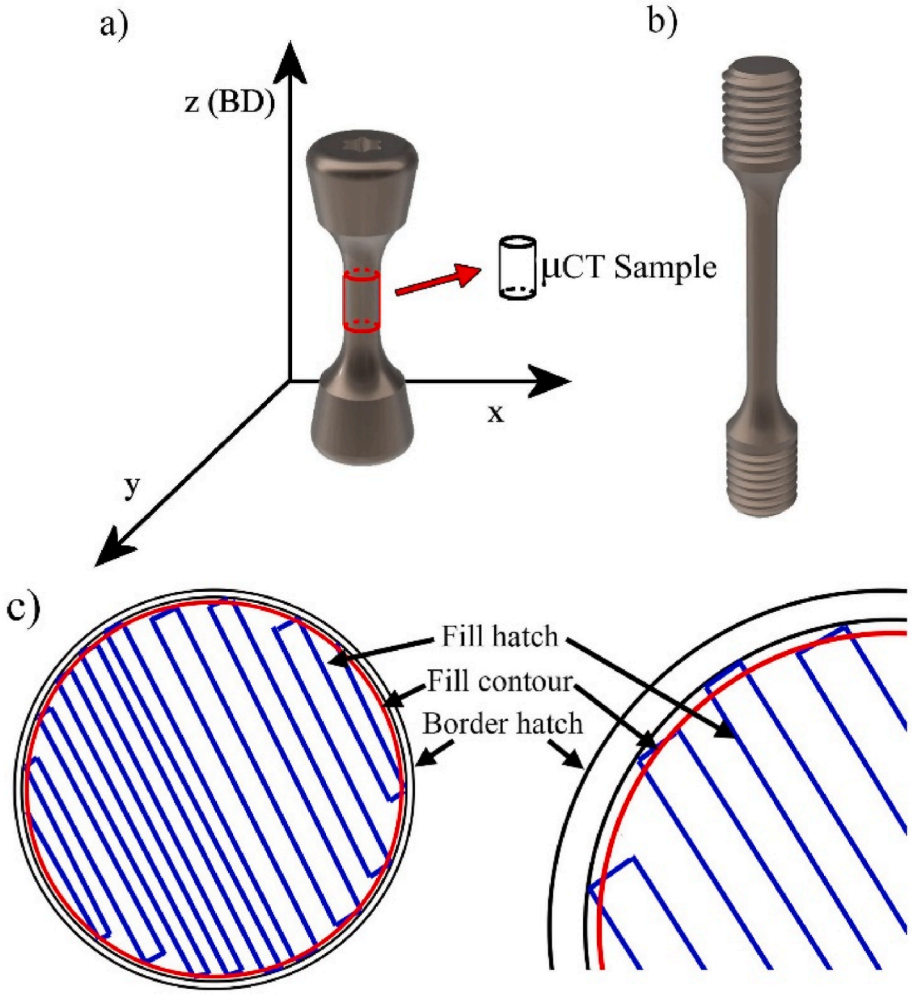

Fig. 1. (a) Macrograph depicting the axial fatigue sample fabricated using the PBF-LB technique, highlighting the geometry, building direction, and the volume of the micro-computed tomography (μCT) sample, (b) tensile sample geometry and (c) a schematic showing the relevant laser scan tracks for building a layer.

columnar structure (Fig. 3b and c). In the H-VED structure (Fig. 2c and 3c), epitaxial grain growth has occurred and remelting of several layers leading to the formation of long columnar grains. An intriguing observation is the evident grain coarsening with increasing the applied VED. Table 3 presents the measured equivalent diameters of the grains, determined by elliptical fitting for each grain's area in the promoted microstructures at various VEDs. The equivalent diameter increases from approximately 81 to 115 μm with the increased printing energy from 50.8 to 84 J/mm^3. If the maximum Feret's diameter is compared, indicating the maximum length of a measured grain, the size increases from 162 to 245 μm, indicating more elongated shape of the grains with increasing VED.

3.2. *Micro-computed tomography (μCT) analysis of defect structure*

The defect structure of the three structures was analysed by the μCT in detail. For illustrating the distribution of the defects across the measured cylinder, Fig. 4 displays the location of all defects in an XY-plane of the sample. Two facts are obvious from this 2D representation: the defect density decreases with increasing VED and a distinct defect-denser zone exists in the subsurface region of a sample. Further, the subsurface location seems non-symmetrical, particularly in the H-VED structure. Presumably the grinding prior polishing caused this asymmetricity, or the process conditions were non-optimal [31,52].

Since the contrast between the defects and the bulk material was high in μCT measurements, segmentation was performed by simple thresholding. Delineated, individual defects were characterized by two shape descriptors: the diameter of the equivalent sphere and the

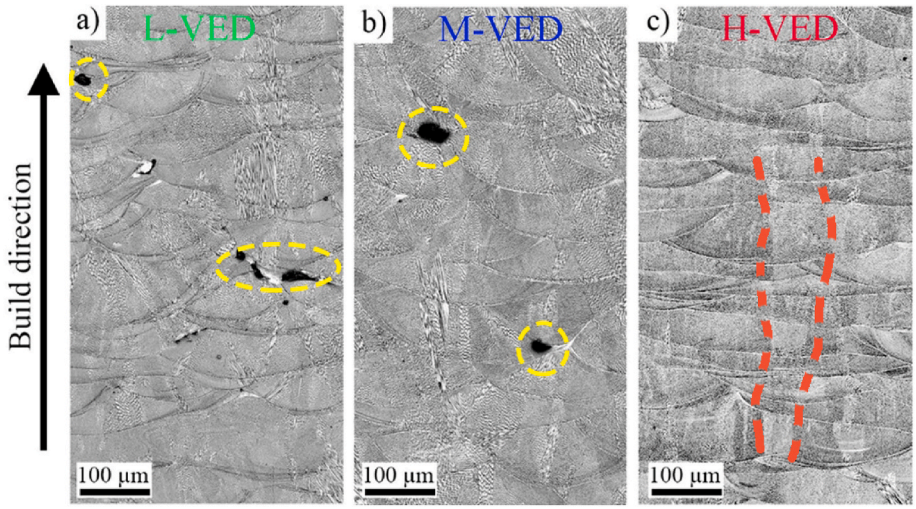

Fig. 2. Microstructure of the as-built 316L steel printed at various VEDs, as captured by laser confocal scanning microscopy: (a) L-VED, (b), M-VED, and (c) H-VED. Some defects are encircled by yellow line. Red dashed lines in (c) indicated the columnar growth through the deposited layers. (For interpretation of the references to colour in this figure legend, the reader is referred to the Web version of this article.)

Table 3
Measured average melt pool and grain sizes, and the densities obtained by the Archimedes' method for the printed 316L structures.

ID	Melt Pool Size [µm]			Grain Size (EBSD) [µm]		Density [%]
	Width	Height	Eq. diam.	Eq. diam.	Max. Feret's diameter	Archimedes' method
L-VED	148	46	85	81	162	91.90
M-VED	166	57	93	108	202	98.92
H-VED	190	55	95	115	245	99.60
Wrought	–	–	–	62	70	100

complexity factor. The former was derived from the total volume of a defect, and the latter was calculated as described by Isaac et al. [53]. Then, a combination of morphological operations (dilation, erosion) was used to extract the bulk material without defects, and these results are plotted in Fig. 5. As is seen from Fig. 5a, all structures contain defects with the complexity factor about 0.4, although it seems that the most complex defects are decreasing in number with the increased VED. If the outliers are considered, the L-VED has the largest deviation in the complexity. Fig. 5b shows the size distribution of the measured defects. The mean defect sizes are almost equal between the structures, but the maximum sizes are the largest for the L-VED structure, the maximum defect diameter being 76 µm. The maximum defect sizes decrease with increasing VED, the maximum diameters being 54 and 50 µm for the M-VED and H-VED structures, respectively.

Segmentation also allowed to compute the distance map, with 0 at the sample surface and maximum value in the core. The density distribution plot is presented in Fig. 6. First, it is obvious that the volume fraction of defects is much higher in the L-VED structure compared to the others. From the distribution, it can be further confirmed that the L-VED and M-VED structures show a peak about 200–250 µm from the polished surface, i.e., about 300 µm from the original printed surface. In the H-VED it is still closer to the surface, but the peak is relatively low.

For a more detailed view, Fig. 7 presents isometric views of 3D reconstructions showcasing the defects within the cubic volume of the three PBF-LB 316L structures. In this representation, the identified defects are visually represented above the measured volume of 7 x 7 × 7 mm^3. A most notable observation is the presence of a high density of defects (depicted in green) with a diverse range of sizes in the L-VED structure. Moreover, the tomography of the L-VED reveals various defect

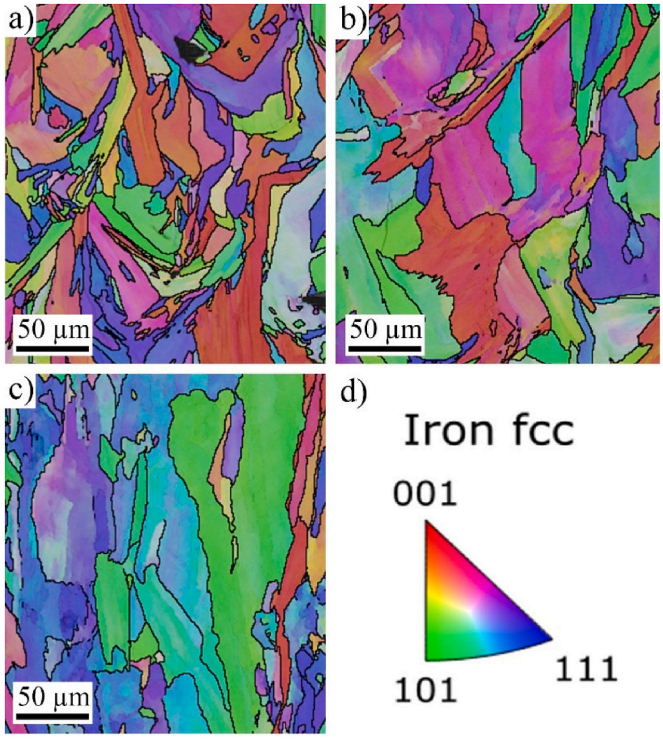

Fig. 3. EBSD-IPF maps of 316L steel printed with different VEDs seen parallel to BD. (a) L-VED, (b) M-VED, (c) H-VED and (d) IPF colour legend. (For interpretation of the references to colour in this figure legend, the reader is referred to the Web version of this article.)

shapes, including spherical, ellipsoidal, and rod-like morphologies, consistently with the wide complexity range shown in Fig. 5a. The defect density and size decrease with increasing VED, and in the H-VED structure, tiny and equiaxed pores are predominant, although one bigger defect was present.

3.3. Mechanical properties

3.3.1. Tensile strength

Quasistatic properties of studied materials are already presented by

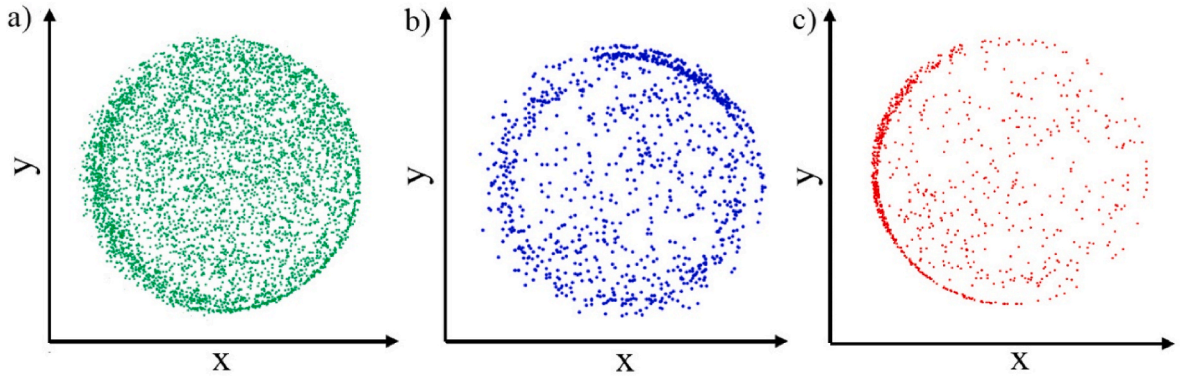

Fig. 4. X-Y plane projection of the location of defects in Z-direction of (a) L-VED, (b) M-VED and (c) H-VED structures.

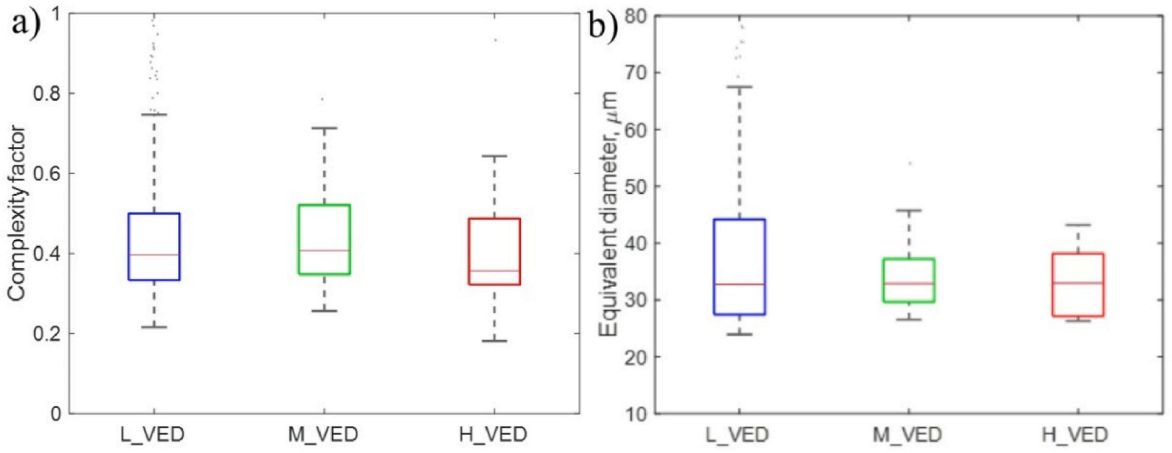

Fig. 5. Box plot representation of complexity factor (a) and an equivalent diameter (b) distribution within the 1 mm from the axis of the sample. Note that each box is defined by 25th, 50th and 75th percentile and whiskers extend to cover 99.7 % of the data (3σ for normal distribution).

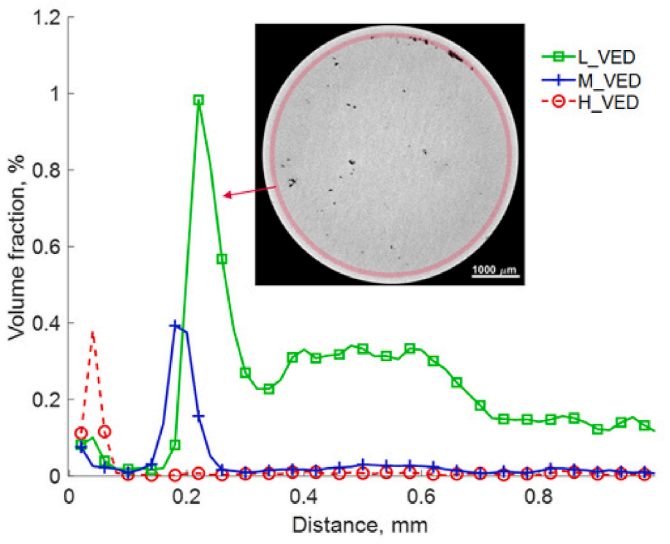

Fig. 6. Void volume fraction distribution as a function of distance from the surface. A sectional view explains the peak for the L-VED sample.

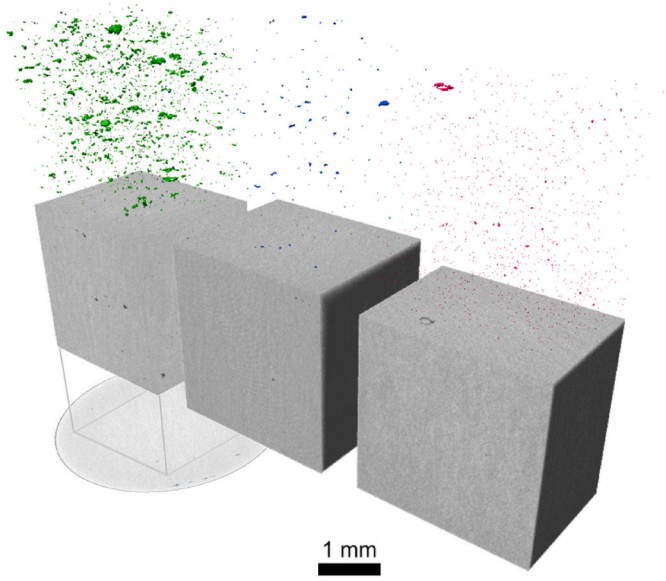

Fig. 7. 3D rendering of acquired tomograms of PBF-LB 316L. Volumes were cropped as indicated by the underlying transverse section for better visualization of internal topology. Segmented voids are presented in different colours for clarity. From left to right: L-VED, M-VED, and H-VED. (For interpretation of the references to colour in this figure legend, the reader is referred to the Web version of this article.)

the author in previous study [24], but as a clarification, properties extracted from the tensile stress-strain curves, such as yield strength (YS), ultimate tensile strength (UTS), uniform elongation (UE), and total elongation (TE) with measured hardness values, are listed as a table

form in Table 4. Notably, the L-VED exhibited high UTS, but lower elongation compared to those of the M-VED and H-VED. For instance, the UTS and TE of L-VED are 610 MPa and 33 %, respectively, while the corresponding values for H-VED are 560 MPa and 48 %. This indicates that more a pronounced softening mechanism promoted in the structures printed at the higher VEDs. A higher heat energy imparted to the printed structure leads to coarsening of the grain structure. The YS values (440–475 MPa) of the printed materials are notably higher than that (402 MPa) of the wrought 316L. Conversely, the UTS and TE of the wrought 316L are higher than those of the printed materials, being 624 MPa and 54 %, respectively. Elongation increases with increasing VED apparently due to of the substructure and lower porosity of the material, as suggested in our previous study [24].

3.3.2. Fatigue strength

The influence of surface roughness on the fatigue resistance of AM metallic materials is well-documented, e.g., Refs. [54–56]. To mitigate the roughness effect, the samples underwent a gentle grinding and electropolishing to remove partially melted powder adhered to the surface before fatigue testing. Also, the stress relieving treatment was performed at 600 °C for 120 min. Fig. 8 presents the analysis of experimental fatigue test data in the form of nominal stress amplitude vs. the number of cycles to failure (S–N) plots up to 10^7 cycles for the three structures deposited with different VEDs. Two noteworthy trends emerge from the S-N curves. Firstly, the fatigue life and strength of the three sets exhibit a slightly increasing trend with the increased VED. For instance, at a stress amplitude of 200 MPa, the corresponding fatigue lives are 0.5×10^5, 1×10^5, and 5×10^5 cycles for the L-VED, M-VED, and H-VED, respectively. However, the FLs (i.e., the stress amplitude at which no failure occurred within 10^7 cycles for 50 % of the samples) of the three sets are closely clustered in the range of 80–100 MPa. In comparison, the FL of the wrought 316L is distinctly higher at 256 MPa. This is consistent for instance with the findings of Hamada et al. [47], who reported a low fatigue limit of 75 MPa for AM 316L printed with a low VED of 40 J/mm^3. At higher stress amplitudes in the LCF regime, the fatigue strength of the M-VED and H-VED printed structures remain comparable or even better than that of the wrought 316L. However, the L-VED structure still seems to have lower fatigue strength even in this regime.

3.3.3. Crack initiation and propagation

Examination of the fracture surfaces after fatigue testing provided insights into crack initiation sites and the type of crack propagation. A careful analysis revealed that fatigue cracks initiated at LoF defects between deposited layers and relatively large defects located in the surface layer of fatigued specimens (note that about 0.1 mm was polished off), even though the majority of defects resided in sub-surface regions, as shown in Fig. 6. Fig. 9a highlights a primary crack initiation site, referred to as the “killer”, denoted by a dashed semi-circle on the fracture surface of a fatigued L-VED 316L sample. A semi-circular LoF defect measures around 250 μm in size. Additionally, another LoF defect was observed in proximity to the main killer. Similarly, in Fig. 9b, a LoF defect is evident on the fracture surface of a fatigued M-VED 316L sample, characterized by an elongated shape and a size of approximately

Table 4
Tensile properties and hardness of the PBF-LB 316L structures printed at different VEDs and wrought 316L. Yield Strength (YS), Ultimate Tensile Strength (UTS), Uniform Elongation (UE), and Total Elongation (TE).

Printed 316L	YS [MPa]	UTS [MPa]	UE [%]	TE [%]	Hardness [HV10]
L-VED	462 ± 6	610 ± 6	22.6 ± 0.3	33.2 ± 1.1	211 ± 3
M-VED	456 ± 14	595 ± 13	23.5 ± 0.3	37.3 ± 2.5	218 ± 7
H-VED	437 ± 4	560 ± 4	27.3 ± 0.2	48.3 ± 3.2	210 ± 4
Wrought 316L	402 ± 4	624 ± 2	36.9 ± 0.2	54.0 ± 0.2	197 ± 6

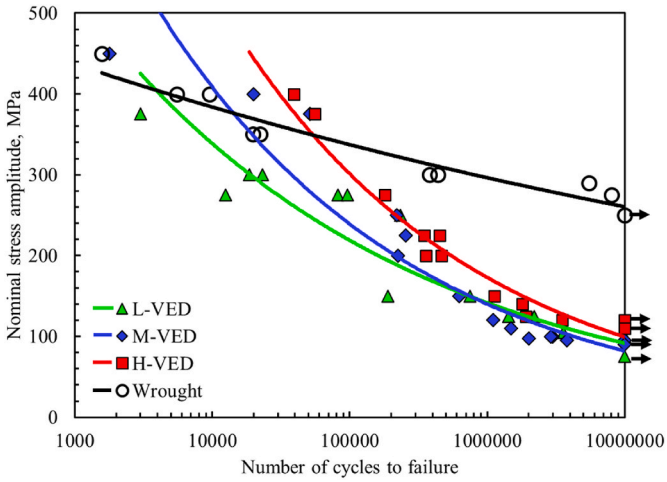

Fig. 8. S-N curves for the 316L structures manufactured with different VEDs and that of a wrought 316L for comparison.

450 μm. In the case of a fatigued H-VED 316L sample, Fig. 9c reveals a subsurface killer, an irregularly shaped LoF defect measuring around 120 μm. These findings align well with established fatigue crack initiation mechanisms observed in several previous studies involving AM 316L structures subjected to cyclic deformation [31,57–60]. The observed crack initiation mechanism underscores the significant role played by process-induced defects, such as LoF, in influencing the fatigue behaviour of 3D printed metallic structures.

Fig. 10 gives examples of the initiation and propagation of fatigue cracks within the fatigued structure. Notably, fatigue cracks can initiate both at a LoF defect, as depicted in Fig. 11a, or a sizable pore, illustrated in Fig. 10b. An intriguing characteristic of zig-zag profile of the crack is observed. This zig-zag pattern emerges as the fatigue crack propagates transgranularly across the cellular grain substructure of a melt pool.

3.3.4. Deformation mechanisms under cyclic straining

To explore the initiation and progression of fatigue cracks in the investigated PBF-LB 316L steel, samples subjected to cyclic loading until failure were cross-sectioned and underwent a gentle grinding and polishing process. Fig. 11 illustrates the deformed microstructure of the L-VED sample formed under cyclic loading at 150 MPa. In Fig. 11a, two initiated microcracks are observed originating from a large irregularly shaped defect, propagating in both right and left directions across subboundaries. This particular defect, due to its irregular shape, acts as a stress concentration site during cyclic straining, forming a favourable site for crack initiation. In Fig. 11b, the Kernel Average Misorientation (KAM) map of the corresponding microstructure is presented to showcase the high degree of misorientation induced by presence of such LoF defect. Highly strained regions, revealed by high KAM values (depicted in green colour), exist around the large LoF defect and along the isthmus between two defects.

The fatigue life of the H-VED 316L structure, fatigued at the stress amplitude of 200 MPa was about 5×10^5 cycles, the longest one among the studied structures (Fig. 9; 4 data points) at this stress amplitude even though it had the lowest strength. Fig. 12a illustrates the local deformation of the structure by showing the presence of parallel deformation bands in two directions within two columnar grains. Zooming in on the highlighted zone in Fig. 12a (a left upper grain) reveals the formation of deformation twins characterized by Σ3 twin boundaries, denoted by the red colour in Fig. 12b. On a higher magnification, the phase map of a lower (right) grain in Fig. 12c reveals that α′-martensite is also present in a tiny amount in the shear band pattern.

In the conducted TEM analysis, a focused examination was performed on the deformation mechanisms within the M-VED sample that underwent cycling to failure at a stress amplitude of 375 MPa (fatigue

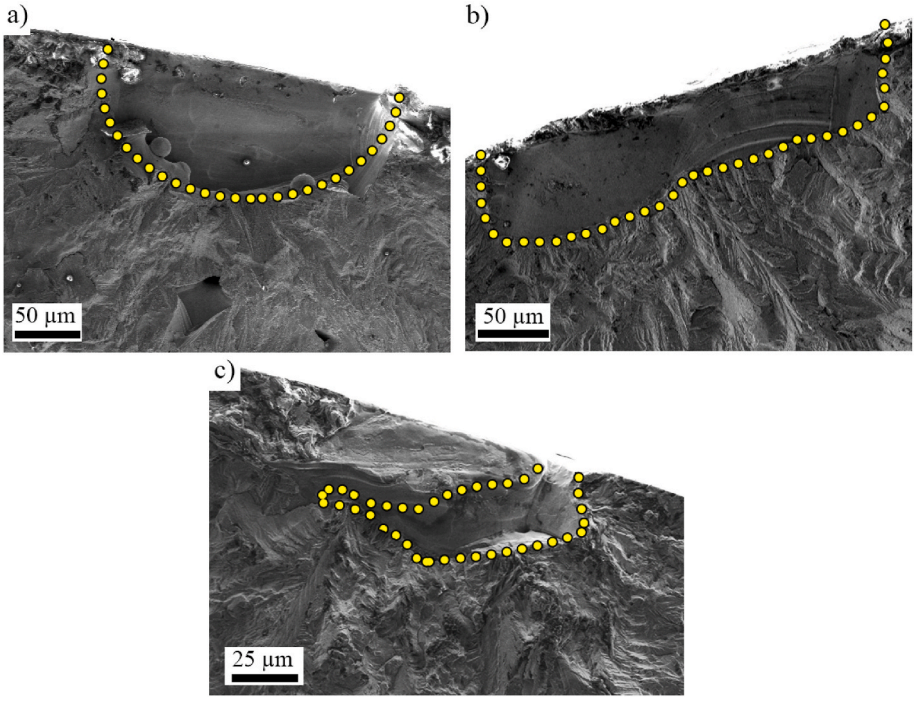

Fig. 9. SEM images depicting fracture surfaces of fatigued LPBF 316L printed at different VEDs: (a) L-VED with an applied stress amplitude of 125 MPa, (b) M-VED with an applied stress amplitude of 100 MPa, (c) H-VED with an applied stress amplitude of 100 MPa. The yellow dashed lines outline the observed defects. (For interpretation of the references to colour in this figure legend, the reader is referred to the Web version of this article.)

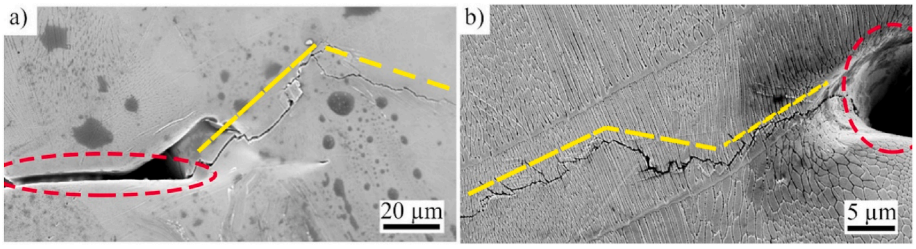

Fig. 10. SEM microstructures capturing the fatigue crack propagation in the L-VED 316L structure at stress amplitude of: (a) 150 MPa and (b) 300 MPa.

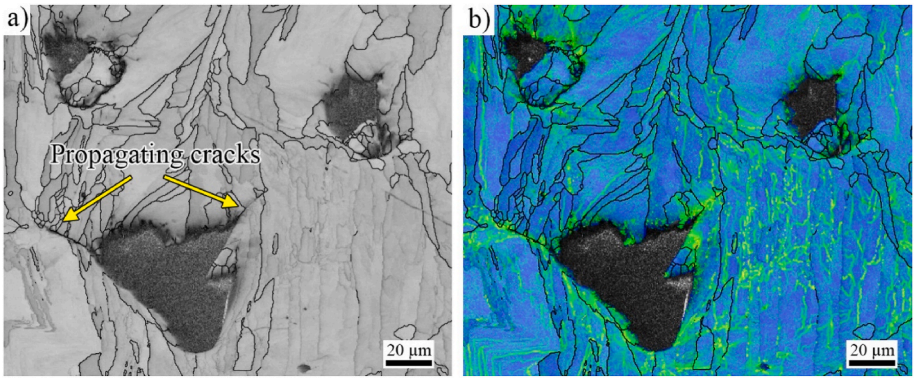

Fig. 11. (a) Band contrast map of clustered LoF defects of L-VED sample fatigued at 150 MPa and (b) KAM map from the same region.

life ≈ 40000 cycles). This examination involved the extraction of a FIB lamella from a region near a cracked LoF defect. The resulting TEM bright-field images, as shown in Fig. 13a, highlighted the presence of parallel sets of twin bundles.

Upon closer inspection of specific locations within the deformed region, the magnified view in Fig. 13b provided further insights. The corresponding Selected Area Electron Diffraction (SAED) pattern in Fig. 13c revealed simultaneous diffractions of deformation twins and ε-martensite, with a specific zone axis [011]γ//[11–20]ε. To elucidate the nature of the deformation, dark field images corresponding to different crystallographic spots were displayed in Fig. 13(d–f). These images demonstrated that the ε-martensite phase formed as thin

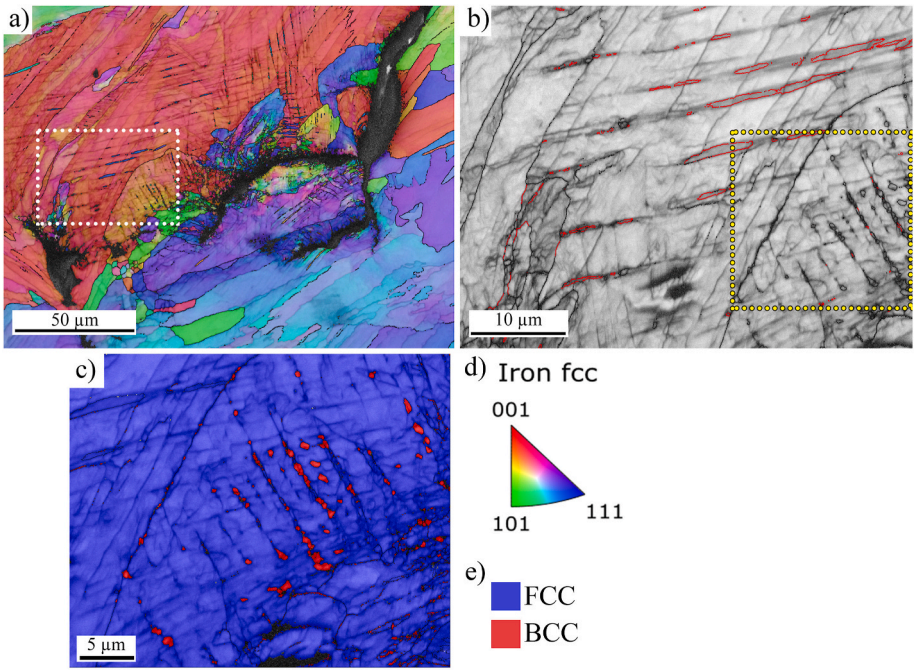

Fig. 12. Microstructural features of the cyclically deformed H-VED 316L at 200 MPa, including (a) EBSD-IPF map, (b) high-magnification EBSD-boundary map of the highlighted zone in (a) revealing mechanical twins in red, and (c) phase map at high magnification of the marked area in (b) displaying austenite in blue and α′-martensite in red. (d) IPF and (e) phase map colour legends. (For interpretation of the references to colour in this figure legend, the reader is referred to the Web version of this article.)

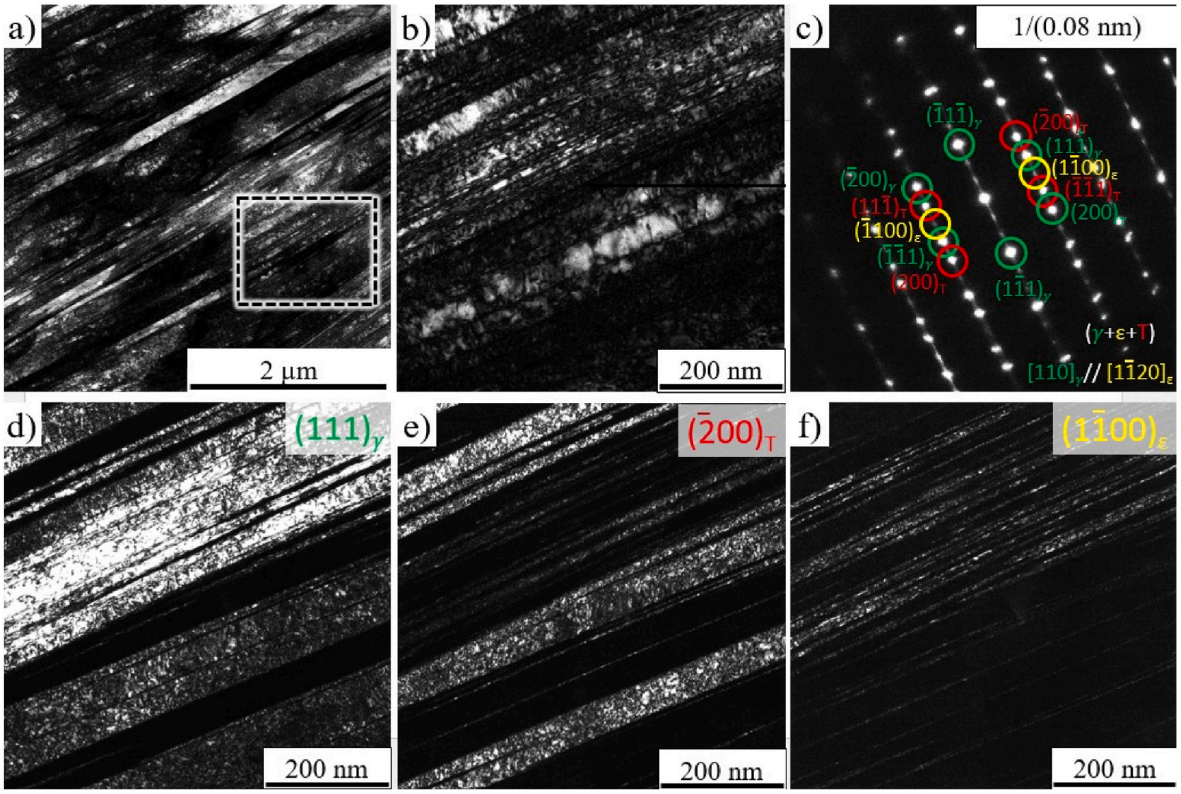

Fig. 13. TEM analysis of deformation mechanism in the fatigued M-VED 316L specimen at 375 MPa stress amplitude. (a) Bright-field TEM image revealing parallel sets of twin bundles. (b) Magnified view of a specific location as marked in (a). (c) Corresponding SAED pattern identifying simultaneous diffractions of deformation twin and ε-martensite with zone axis [011]γ//[11–20]ε. (d–f) Dark field images corresponding to matrix (111), twin (−200), and ε-martensite (1–100) spots, respectively.

platelets on {111} twin planes, aligning with findings of α′-martensite by EBSD.

4. Discussion

4.1. The effect of static properties and microstructure on fatigue strength

It is well-established that the fatigue limits of steels are commonly correlated with their tensile strength, the FL/UTS ratio typically falling between 0.4 and 0.6, or 1.5–1.6 times the material hardness [61]. For comparison of tensile and fatigue properties of the PBF-LB 316L, the experimental values obtained from the present tests are listed in Table 5. From the table, it is seen that for the wrought 316L steel, the FL/UTS ratio is 0.41. However, the PBF-LB 316L structures exhibit significantly lower ratios, ranging from 0.14 to 0.17. The observed low FL (at 10^7 cycles) is consistent with results reported e.g., by Elangeswaran et al. [48] and Cui et al. [62]. This clear deviation indicates that the static strength of the PBF-LB material is not a determinant of its FL in the presence of defects. This aligns with existing literature, as demonstrated in numerous papers in the literature, e.g., Refs. [34,36,47,49,56]. However, if the density of PBF-LB 316L sample is high and major defects are removed by machining the sample, the printed PBF-LB 316L seems to achieve the FL even exceeding that of the wrought 316L steel [48,49].

Scatter in the experimental fatigue life data, most pronounced at 280–300 MPa amplitudes, is most obvious for the L-VED structure (Fig. 9), where the defect fraction was high, and the complexity of defects varied broadly (Fig. 5). However, some differences between the S-N curves in Fig. 9 can be seen, the H-VED exhibiting the longest fatigue life, even though the H-VED had the lowest UTS of the studied structures. The fatigue strength at 10^4 cycles decreases from 470 MPa of the H-VED structure to 340 MPa of the L-VED one, as is depicted in Table 5. This indicates that even in the LCF regime, the deformation mechanisms controlling the UTS only have small effect on fatigue behaviour and the fatigue strength is more related to the ductility. As is shown in the literature [24,63], the higher applied VED increases the TE, allowing enhanced plastic deformation of the softer material. The same might be present in fatigue in the LCF regime, where higher plastic strain amplitudes are present, and ductile material can withstand more local plastic deformation prior crack initiation and growth. The L-VED and M-VED structures have lower ductility due to microstructural features, and partly due to higher defect content, which is seen as impaired elongation and LCF fatigue resistance.

Furthermore, as seen in Figs. 12 and 13, local deformation, promoted by presence of irregular LoF defects, may lead to twinning and phase transformation in PBF-LB 316L despite of its relatively high stacking fault energy (SFE) [24,64,65]. Even though twin boundaries can be preferable sites for crack initiation, twinning and martensite transformation may hinder the crack propagation by introducing obstacles for the crack path, as well as causing local cyclic hardening of the material. In this instance, the occurrence of these specific microstructural features indicate that the M-VED and H-VED structures exhibit increased capacity for accommodating localized strain during cyclic loading compared to the L-VED structure. This was shown previously for similar PBF-LB 316L structure of a machined sample, where slight cyclic hardening occurred during axial fatigue [44]. This in combination with high ductility results in somewhat enhanced fatigue life of the H-VED structure in the LCF regime.

Table 5
Ratios of fatigue limit to Tensile Strength (TS), Fatigue Limit at 50 % probability (FAT50 %), Fatigue Limit at 50 % to Ultimate Tensile Strength ratio (FAT/UTS), and Fatigue Strength at 10^4 cycles (FAT at 10^4) for 316L structures printed at different VEDs and wrought 316L.

Printed 316L	UTS [MPa]	FAT50 % [MPa]	FAT/UTS –	FAT at 10^4 cycles [MPa]	Max. Defect length (LCSM) [μm]
L-VED	610 ± 6	93	0.15	340	394
M-VED	595 ± 13	82	0.14	450	179
H-VED	560 ± 4	97	0.17	470	86
Wrought	624 ± 2	256	0.41	390	–

4.2. The influence of defect structure on fatigue strength

As pointed out, the defects in PBF-LB materials results in low fatigue resistance compared to their static properties. The present results indicate that the increasing VED leads to lower fraction of defects (Fig. 6), slightly smaller defect size and complexity (Fig. 5), and improves slightly the fatigue life, but still the fatigue resistance remains distinctly lower than that of the wrought 316L steel. For emphasizing the influence of defect characteristics, LCSM was employed for measuring the defect sizes on polished cross-sections of large number of samples (10 cross-sections) of each structure, and the results of this examination are shown in Fig. 14. In the L-VED structure, larger and more irregularly shaped defects are prevalent, ranging up to approximately 390 μm. On the other hand, the H-VED structure exhibits smaller and more uniformly shaped defects, with sizes ranging from 5 to 84 μm (according to LCSM).

At higher stress amplitudes, the H-VED structure outperforms the M-VED and L-VED structures in terms of fatigue strength. This improvement can be attributed to the combined effects of a reduced defect fraction, smaller size, and potentially a less complex defect shape in the H-VED structure, in addition to possible local strengthening by twinning and martensite transformation (Figs. 12 and 13), as discussed in the previous section.

The decreased complexity in defect shapes, seen in Fig. 5, contributes to lower stress concentrations along the irregular borders of the defects that leads to enhanced fatigue life [29,52]. Fig. 15 illustrates further the geometric intricacies of defects in both L-VED and H-VED structures. In the L-VED structure (Fig. 15a), LoF defects exhibit irregular shapes with sharp corners, as highlighted by dashed yellow lines. Such defect configurations with sharp corners are identified as crack initiation sites. Conversely, in the H-VED microstructure (Fig. 15b), defects are mostly round, as indicated by yellow circles. Notably, spherical pores do not contribute to the initiation of fatigue cracks, and they are generally also smaller in size [47].

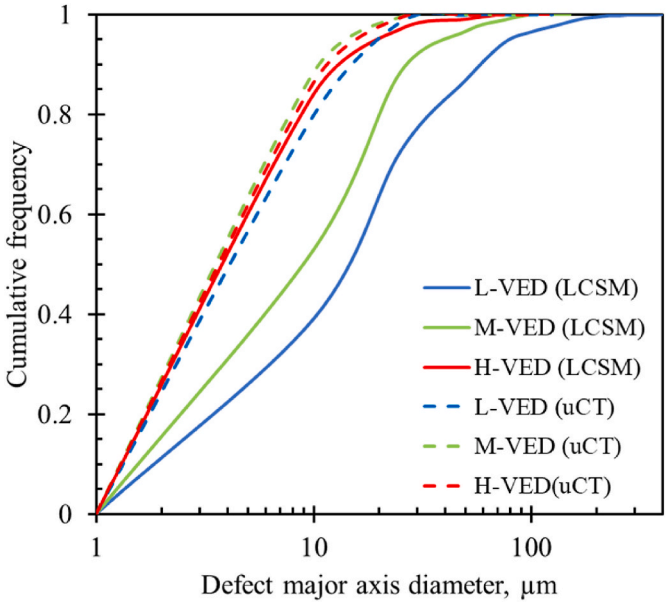

Fig. 14. Defect distributions as cumulative frequencies based on μCT and LCSM data.

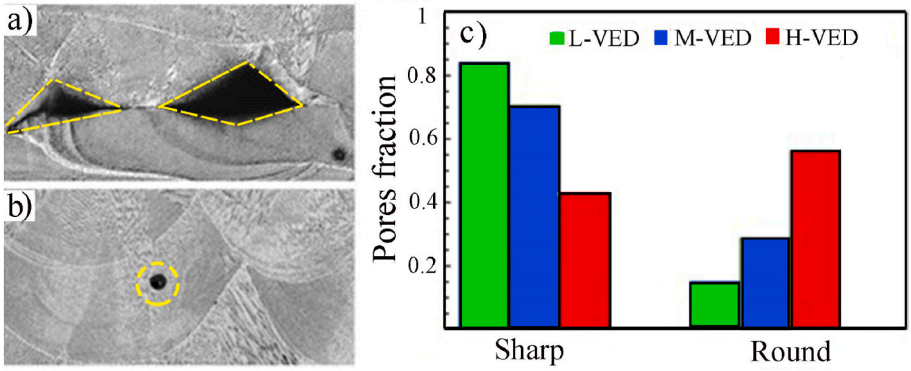

Fig. 15. Illustration of the geometric complexity of defects in VEDs structures. In (a) L-VED microstructure, large defects with irregular shapes and sharp corners (highlighted by dashed yellow lines), (b) H-VED microstructure, round pores, and (c) Statistical analysis of the defect shapes, based on total number of defects. (For interpretation of the references to colour in this figure legend, the reader is referred to the Web version of this article.)

A statistical examination (at least 100 defects from each structure) of defect shapes, conducted using LCSM images on polished cross-sections, revealed that 84 % of the analysed defects in the L-VED structure exhibited sharp shapes. In contrast, the prevalence of sharp defects was notably reduced in the H-VED structure, accounting for about 40 % only (Fig. 15c). This reduction in the percentage of sharp defects in the H-VED structure suggests a mitigation of stress concentration sites, contributing to improved fatigue resistance compared to the L-VED structure.

Another crucial factor influencing on the defect criticality is their location relative to the outer surface, for the significance of a defect depends not only on its size, but also on its proximity to the surface [29, 66]. It is well-established that fatigue cracks tend to initiate at favourable sites on or near the outer surface due to higher local stress concentration. As depicted in Fig. 6, a notable portion of defects in the studied PBF-LB 316L structures were subsurface situated, within approximately 0.2 mm from the outer surface. This distance confines well with the location between the fill contour and the fill hatch. As some material was removed from the surface by gentle polishing, higher number of defects remained near the surface. This proximity to the surface increases the criticality of these defects. In the context of the L-VED structure, the combination of large defect size and intricate shapes as observed from the conducted defect analysis by μCT and LCSM further amplifies the criticality factor. Consequently, the fatigue behaviour of the L-VED structure is comparatively worse than those of the other investigated structures.

Recently, Wang et al. [29]. investigated the influence of defect characteristics, their size, location and shape, on fatigue behaviour of a selective laser melted IN718 alloy. Those characteristics were determined by μCT on machined samples as well as on fracture surfaces of fatigue samples, and they were shown to follow the Gumbel distribution functions. It was demonstrated that the adoption of those three characteristics (size, location and shape) in the stress intensity range enabled to present the fatigue life as a function of the stress intensity threshold value (ΔK_{th}) and reduce the experimental scatter in the S-N data.

The Kitagawa-Takahashi diagram can be applied to show the dependence of FL of a defected structure on defect size [67]. In addition to the hardness of the steel, the stress intensity threshold value for long cracks ($\Delta K_{th,lc}$) is needed for the diagram. Here, for incorporating the measured $(area)^{0.5}$ values to the plot, fracture surfaces of the fatigued H-VED samples were examined, and the area and location of the killer defect were determined. The Kitagawa-Takahashi plot for the H-VED structure is drawn in Fig. 16a. As all failures were surface or subsurface related, the used coefficients were constant in the plot. As can be seen, the experimental data agree with the Kitagawa-Takahashi plot with $\Delta K_{th,lc}$ of 2.5 MPa*$m^{0.5}$. Riemer et al. [68]and Fergani et al. [69] studied the crack growth behaviour of PBF-LB 316L, and they also presented low

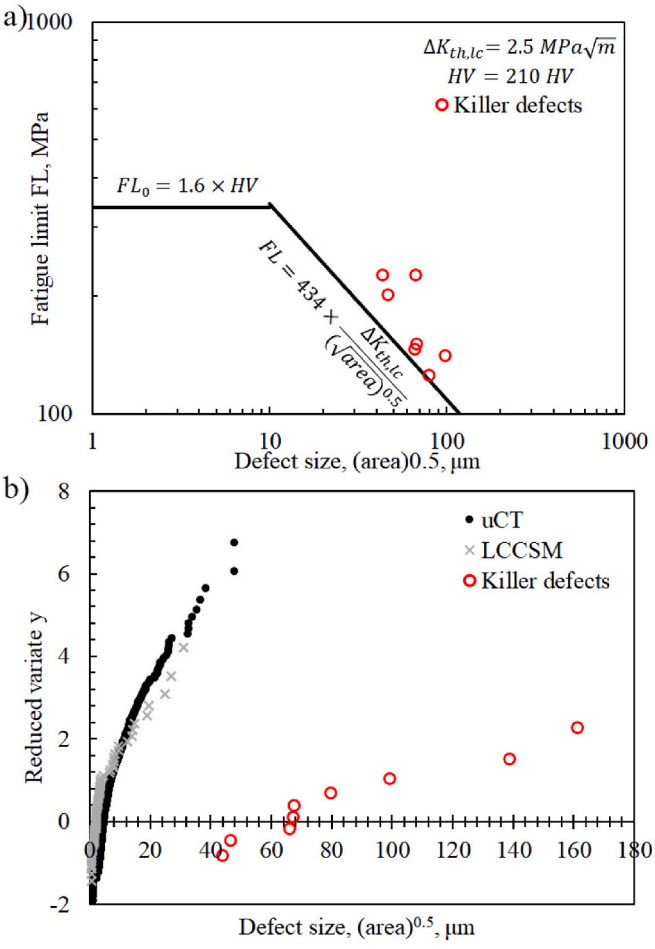

Fig. 16. (a) Kitagawa-Takahashi plot for the H-VED structure including the low ΔK_{th} threshold value and (b) Gumbel-plot of the defect $(area)^{0.5}$ parameter distribution acquired from μCT, and LCSM on polished cross-sections and fracture surface examinations.

ΔK_{th} values of 3 MPa*$m^{0.5}$.

In Fig. 16b, the Gumbel extreme value distributions for the defects size, based on μCT and LCSM analyses both on cross-sections and fracture surface, are shown. Reduced variate y is calculated using equations

$$F_j = \frac{j \bullet 100}{n+1}, \quad (2)$$

$$y = -\ln\left[-\ln\left(\frac{F_j}{n+1}\right)\right], \quad (3)$$

where Fj is the cumulative distribution function of defects, j is the number of the defect and n is the total number of defects. The μCT and LCSM on cross-sections are in fair agreement, but the killer defect distribution on fracture surfaces deviates significantly from them. This means that the crack-initiated area for the defect size is larger on fracture surface than in the μCT data, which is the maximum value in a measured cross section, not necessarily the largest defect in the whole specimen. This was also pointed out by Wang et al. [29].

Concerning the FL, it can be concluded that even a small amount of porosity is enough to decrease the FL considerably from the ideal one, meaning that the defect size and shape are the most important factors regarding the fatigue life of PBF-LB 316L. Even though the defect size distributions are smaller in the M-VED and H-VED structures, and the number is greatly lower, still the crack initiation can occur in LoF type defects, as was shown in the SEM images in Figs. 9 and 10.

The present results indicate that even in the printed material with the density of 99.6 % achievable by a high VED, some subsurface defects are still present and significantly reduce the fatigue life at small stress amplitudes. However, it is known that after machining the sample, the FL exceeding that of the wrought steel can be obtained [48,49]. Therefore, future studies are needed to solve this dilemma.

5. Conclusions

This comprehensive investigation delves into the complex interplay between axial fatigue life and the laser beam powder bed fusion (PBF-LB) manufacturing process, specifically in an AISI 316L type austenitic stainless steel. The exploration of three volumetric energy densities (VEDs) - low (50.8 J/mm^3), medium (79.4 J/mm^3), and high (84.3 J/mm^3) with densities from 91.8 to 99.6 % - sheds light on their profound influence on the defect level and characteristics within 3D printed structures. The key findings and conclusions drawn from this study are summarized as follows:

1. The fraction and size of defects decreased with increasing VED, the high VED structure exhibiting more homogenous and consolidated size distribution. The number of roundish gas pores increased with increasing VED. However, still 40 % of defects were the lack of fusion type even in high VED structure.
2. The micro-computed tomography analysis revealed that defects distribution across the investigated samples exhibited a distinct subsurface peak about 0.2 mm from the polished surface, after grinding and polishing about 0.1 mm off from the original surface. This is obviously connected with the deposited border hatch and fill contour.
3. All defect characteristics contributed to distinct reduction of fatigue strength in the HCF regime. All the structures exhibited the low fatigue limit in the range 80–100 MPa. However, the fatigue limits are dictated by the largest defect in the specimen which role was modelled by the Murakami's (area)$^{0.5}$ parameter approach for the high VED structure. This led to a low ΔK_{th} value of 2.5 MPa*m$^{0.5}$.
4. LoF type killer defects observed on fatigue fracture surfaces were much larger than defects classified by micro-computed tomography and microscopically on polished cross-sections, even in the high VED structure.
5. The results indicate that for achieving a fatigue limit equal to that of the wrought alloy, special emphasis is required to deposit a defect-free alloy, with a high VED, if machining of the surface layer (0.3 mm or more) is not feasible.

CRediT authorship contribution statement

Matias Jaskari: Writing – original draft, Methodology, Investigation, Conceptualization. **Atef Hamada:** Writing – review & editing, Investigation. **Tarek Allam:** Writing – original draft, Investigation. **Krzysztof Dzieciol:** Writing – original draft, Investigation. **Sumit Ghosh:** Writing – original draft, Investigation. **Ruth Schwaiger:** Writing – review & editing, Formal analysis. **Pentti Karjalainen:** Writing – review & editing, Supervision. **Antti Järvenpää:** Writing – review & editing, Supervision, Funding acquisition.

Declaration of competing interest

The authors declare that they have no known competing financial interests or personal relationships that could have appeared to influence the work reported in this paper.

Acknowledgement

The authors express their gratitude to the BUSINESS Finland for funding this research through "DREAMS" project, No. 4795/31/2021. Part of the examinations have been conducted using the equipment of Centre of Material Analysis, University of Oulu.

Data availability

Data will be made available on request.

References

[1] K. Mäntyjärvi, T. Iso-Junno, H. Niemi, J. Mäkikangas, Design for additive manufacturing in extended DFMA process, Key Eng. Mater. 786 (2018) 342–347. https://doi.org/10.4028/www.scientific.net/kem.786.342.
[2] M.K. Thompson, G. Moroni, T. Vaneker, G. Fadel, R.I. Campbell, I. Gibson, A. Bernard, J. Schulz, P. Graf, B. Ahuja, F. Martina, Design for additive manufacturing: trends, opportunities, considerations, and constraints, CIRP Ann. - Manuf. Technol. 65 (2016) 737–760, https://doi.org/10.1016/j.cirp.2016.05.004.
[3] W. Abd-Elaziem, S. Elkatatny, A.E. Abd-Elaziem, M. Khedr, M.A. Abd El-Baky, M. A. Hassan, M. Abu-Okail, M. Mohammed, A. Järvenpää, T. Allam, A. Hamada, On the current research progress of metallic materials fabricated by laser powder bed fusion process: a review, J. Mater. Res. Technol. 20 (2022) 681–707, https://doi.org/10.1016/J.JMRT.2022.07.085.
[4] A. Strondl, O. Lyckfeldt, H. Brodin, U. Ackelid, Characterization and control of powder properties for additive manufacturing, Jom 67 (2015) 549–554, https://doi.org/10.1007/s11837-015-1304-0.
[5] R. Li, Y. Shi, Z. Wang, L. Wang, J. Liu, W. Jiang, Densification behavior of gas and water atomized 316L stainless steel powder during selective laser melting, Appl. Surf. Sci. 256 (2010) 4350–4356, https://doi.org/10.1016/j.apsusc.2010.02.030.
[6] S. Zhang, Q.S. Wei, G.K. Lin, X. Zhao, Y.S. Shi, Effects of powder characteristics on selective laser melting of 316L stainless steel powder, in: Manufacturing Process Technology, 2011, pp. 3664–3667. https://doi.org/10.4028/www.scientific.net/AMR.189-193.3664.
[7] J.P. Oliveira, A.D. LaLonde, J. Ma, Processing parameters in laser powder bed fusion metal additive manufacturing, Mater. Des. 193 (2020) 108762, https://doi.org/10.1016/J.MATDES.2020.108762.
[8] L. Thijs, F. Verhaeghe, T. Craeghs, J. Van Humbeeck, J.P. Kruth, A study of the microstructural evolution during selective laser melting of Ti–6Al–4V, Acta Mater. 58 (2010) 3303–3312, https://doi.org/10.1016/J.ACTAMAT.2010.02.004.
[9] J. Haubrich, J. Gussone, P. Barriobero-Vila, P. Kürnsteiner, E.A. Jägle, D. Raabe, N. Schell, G. Requena, The role of lattice defects, element partitioning and intrinsic heat effects on the microstructure in selective laser melted Ti-6Al-4V, Acta Mater. 167 (2019) 136–148, https://doi.org/10.1016/J.ACTAMAT.2019.01.039.
[10] U. Scipioni Bertoli, A.J. Wolfer, M.J. Matthews, J.P.R. Delplanque, J. M. Schoenung, On the limitations of volumetric energy density as a design parameter for selective Laser melting, Mater. Des. 113 (2017) 331–340, https://doi.org/10.1016/J.MATDES.2016.10.037.
[11] T. Rautio, H. Torbati-Sarraf, T. Allam, A. Järvenpää, A. Hamada, Enhancement of electrical conductivity and corrosion resistance by gold-nickel coating of additively manufactured AlSi10Mg alloy, J. Mater. Res. Technol. 17 (2022) 521–536, https://doi.org/10.1016/J.JMRT.2022.01.022.
[12] T. Rautio, A. Hamada, J. Kumpula, A. Järvenpää, T. Allam, Enhancement of electrical conductivity and corrosion resistance by silver shell-copper core coating of additively manufactured AlSi10Mg alloy, Surf. Coat. Technol. 403 (2020) 126426, https://doi.org/10.1016/J.SURFCOAT.2020.126426.
[13] R. Zhao, C. Chen, W. Wang, T. Cao, S. Shuai, S. Xu, T. Hu, H. Liao, J. Wang, Z. Ren, On the role of volumetric energy density in the microstructure and mechanical

properties of laser powder bed fusion Ti-6Al-4V alloy, Addit. Manuf. 51 (2022) 102605, https://doi.org/10.1016/J.ADDMA.2022.102605.
[14] K.G. Prashanth, S. Scudino, T. Maity, J. Das, J. Eckert, Is the energy density a reliable parameter for materials synthesis by selective laser melting? Mater. Res. Lett. 5 (2017) 386–390, https://doi.org/10.1080/21663831.2017.1299808.
[15] A. Leicht, M. Rashidi, U. Klement, E. Hryha, Effect of process parameters on the microstructure, tensile strength and productivity of 316L parts produced by laser powder bed fusion, Mater. Char. 159 (2020) 110016, https://doi.org/10.1016/j.matchar.2019.110016.
[16] J.A. Cherry, H.M. Davies, S. Mehmood, N.P. Lavery, S.G.R. Brown, J. Sienz, Investigation into the effect of process parameters on microstructural and physical properties of 316L stainless steel parts by selective laser melting, Int. J. Adv. Des. Manuf. Technol. 76 (2015) 869–879, https://doi.org/10.1007/s00170-014-6297-2.
[17] H. Choo, K.L. Sham, J. Bohling, A. Ngo, X. Xiao, Y. Ren, P.J. Depond, M. J. Matthews, E. Garlea, Effect of laser power on defect, texture, and microstructure of a laser powder bed fusion processed 316L stainless steel, Mater. Des. 164 (2019), https://doi.org/10.1016/j.matdes.2018.12.006.
[18] T. Larimian, M. Kannan, D. Grzesiak, B. AlMangour, T. Borkar, Effect of energy density and scanning strategy on densification, microstructure and mechanical properties of 316L stainless steel processed via selective laser melting, Mater. Sci. Eng., A 770 (2020) 138455, https://doi.org/10.1016/J.MSEA.2019.138455.
[19] M.A. Buhairi, F.M. Foudzi, F.I. Jamhari, A.B. Sulong, N.A.M. Radzuan, N. Muhamad, I.F. Mohamed, A.H. Azman, W.S.W. Harun, M.S.H. Al-Furjan, Review on volumetric energy density: influence on morphology and mechanical properties of Ti6Al4V manufactured via laser powder bed fusion, Progress Addit. Manufact. 2022 (2022) 1–19, https://doi.org/10.1007/S40964-022-00328-0.
[20] F. Caiazzo, V. Alfieri, G. Casalino, On the relevance of volumetric energy density in the investigation of Inconel 718 laser powder bed fusion, Materials 13 (2020) 538, https://doi.org/10.3390/MA13030538, 13 (2020) 538.
[21] J.C. Hastie, M.E. Kartal, L.N. Carter, M.M. Attallah, D.M. Mulvihill, Classifying shape of internal pores within AlSi10Mg alloy manufactured by laser powder bed fusion using 3D X-ray micro computed tomography: influence of processing parameters and heat treatment, Mater. Char. 163 (2020) 110225, https://doi.org/10.1016/J.MATCHAR.2020.110225.
[22] N. Sanaei, A. Fatemi, Defects in additive manufactured metals and their effect on fatigue performance: a state-of-the-art review, Prog. Mater. Sci. 117 (2021) 100724, https://doi.org/10.1016/J.PMATSCI.2020.100724.
[23] E.W. Jost, J.C. Miers, A. Robbins, D.G. Moore, C. Saldana, Effects of spatial energy distribution-induced porosity on mechanical properties of laser powder bed fusion 316L stainless steel, Addit. Manuf. 39 (2021) 101875, https://doi.org/10.1016/J.ADDMA.2021.101875.
[24] M. Jaskari, S. Ghosh, I. Miettunen, P. Karjalainen, A. Järvenpää, Tensile properties and deformation of AISI 316l additively manufactured with various energy densities, Materials 14 (2021) 5809.
[25] A. Röttger, J. Boes, W. Theisen, M. Thiele, C. Esen, A. Edelmann, R. Hellmann, Microstructure and mechanical properties of 316L austenitic stainless steel processed by different SLM devices, Int. J. Adv. Des. Manuf. Technol. 108 (3) (2020) 769–783, https://doi.org/10.1007/S00170-020-05371-1, 108 (2020).
[26] G.S. Ponticelli, R. Panciroli, S. Venettacci, F. Tagliaferri, S. Guarino, Experimental investigation on the fatigue behavior of laser powder bed fused 316L stainless steel, CIRP J. Manuf Sci. Technol. 38 (2022) 787–800, https://doi.org/10.1016/J.CIRPJ.2022.07.007.
[27] Y. Cao, Z. Moumni, J. Zhu, Y. Zhang, Y. You, W. Zhang, Comparative investigation of the fatigue limit of additive-manufactured and rolled 316 steel based on self-heating approach, Eng. Fract. Mech. 223 (2020) 106746, https://doi.org/10.1016/J.ENGFRACMECH.2019.106746.
[28] S. Beretta, S. Romano, A comparison of fatigue strength sensitivity to defects for materials manufactured by AM or traditional processes, Int. J. Fatig. 94 (2017) 178–191, https://doi.org/10.1016/J.IJFATIGUE.2016.06.020.
[29] M.L. Wang, X.G. Yang, B. Li, D.Q. Shi, G.L. Miao, S.Q. Guo, Y.S. Fan, The dominant role of defects on fatigue behaviour of a SLM Ni-based superalloy at elevated temperature, Int. J. Fatig. 176 (2023) 107894, https://doi.org/10.1016/j.ijfatigue.2023.107894.
[30] X. Liang, A. Hor, C. Robert, M. Salem, F. Lin, F. Morel, High cycle fatigue behavior of 316L steel fabricated by laser powder bed fusion: effects of surface defect and loading mode, Int. J. Fatig. 160 (2022) 106843, https://doi.org/10.1016/J.IJFATIGUE.2022.106843.
[31] O. Andreau, E. Pessard, I. Koutiri, P. Peyre, N. Saintier, Influence of the position and size of various deterministic defects on the high cycle fatigue resistance of a 316L steel manufactured by laser powder bed fusion, Int. J. Fatig. 143 (2021) 105930, https://doi.org/10.1016/J.IJFATIGUE.2020.105930.
[32] S. Romano, P.D. Nezhadfar, N. Shamsaei, M. Seifi, S. Beretta, High cycle fatigue behavior and life prediction for additively manufactured 17-4 PH stainless steel: effect of sub-surface porosity and surface roughness, Theor. Appl. Fract. Mech. 106 (2020) 102477, https://doi.org/10.1016/j.tafmec.2020.102477.
[33] K. Solberg, S. Guan, S.M.J. Razavi, T. Welo, K.C. Chan, F. Berto, Fatigue of additively manufactured 316L stainless steel: the influence of porosity and surface roughness, Fatig. Fract. Eng. Mater. Struct. 42 (2019) 2043–2052, https://doi.org/10.1111/ffe.13077.
[34] M. Jaskari, J. Mäkikangas, A. Järvenpää, K. Mäntyjärvi, P. Karjalainen, Effect of high porosity on bending fatigue properties of 3D printed AISI 316L steel, Procedia Manuf. 36 (2019) 33–41.
[35] J. Wang, M. Zhang, B. Wang, X. Tan, W.J. Wu, Y. Liu, G.J. Bi, S.B. Tor, E. Liu, Influence of surface porosity on fatigue life of additively manufactured ASTM A131 EH36 steel, Int. J. Fatig. 142 (2021) 105894, https://doi.org/10.1016/j.ijfatigue.2020.105894.
[36] C. Ye, C. Zhang, J. Zhao, Y. Dong, Effects of post-processing on the surface finish, porosity, residual stresses, and fatigue performance of additive manufactured metals: a review, J. Mater. Eng. Perform. 30 (9) (2021) 6407–6425, https://doi.org/10.1007/S11665-021-06021-7, 30 (2021).
[37] Y. Yamashita, T. Murakami, R. Mihara, M. Okada, Y. Murakami, Defect analysis and fatigue design basis for Ni-based superalloy 718 manufactured by selective laser melting, Int. J. Fatig. 117 (2018) 485–495, https://doi.org/10.1016/J.IJFATIGUE.2018.08.002.
[38] M. Zhang, C.N. Sun, X. Zhang, P.C. Goh, J. Wei, D. Hardacre, H. Li, Fatigue and fracture behaviour of laser powder bed fusion stainless steel 316L: influence of processing parameters, Mater. Sci. Eng., A 703 (2017) 251–261, https://doi.org/10.1016/J.MSEA.2017.07.071.
[39] W. Zhu, Z. Moumni, J. Zhu, Y. Zhang, S. Li, W. Zhang, A multi-scale experimental investigation for fatigue limit and fatigue crack initiation behavior of powder bed fusion-laser beam 316L stainless steel, Mater. Sci. Eng., A 866 (2023) 144692, https://doi.org/10.1016/J.MSEA.2023.144692.
[40] R. Douglas, W. Beard, N. Barnard, S. Lee, S. Shao, N. Shamsaei, T. Jones, R. Lancaster, The influence of energy density on the low cycle fatigue behaviour of laser powder bed fused stainless steel 316L, Int. J. Fatig. 181 (2024) 108123, https://doi.org/10.1016/J.IJFATIGUE.2023.108123.
[41] R. Shrestha, J. Simsiriwong, N. Shamsaei, Fatigue behavior of additive manufactured 316L stainless steel under axial versus rotating-bending loading: synergistic effects of stress gradient, surface roughness, and volumetric defects, Int. J. Fatig. 144 (2021) 106063, https://doi.org/10.1016/J.IJFATIGUE.2020.106063.
[42] R. Shrestha, J. Simsiriwong, N. Shamsaei, Fatigue behavior of additive manufactured 316L stainless steel parts: effects of layer orientation and surface roughness, Addit. Manuf. 28 (2019) 23–38, https://doi.org/10.1016/J.ADDMA.2019.04.011.
[43] R. Shrestha, J. Simsiriwong, N. Shamsaei, Fatigue behavior of additive manufactured 316L stainless steel parts: effects of layer orientation and surface roughness, Addit. Manuf. 28 (2019) 23–38, https://doi.org/10.1016/J.ADDMA.2019.04.011.
[44] P. Kumar, R. Jayaraj, J. Suryawanshi, U.R. Satwik, J. McKinnell, U. Ramamurty, Fatigue strength of additively manufactured 316L austenitic stainless steel, Acta Mater. 199 (2020) 225–239, https://doi.org/10.1016/J.ACTAMAT.2020.08.033.
[45] B. Blinn, F. Krebs, M. Ley, R. Teutsch, T. Beck, Determination of the influence of a stress-relief heat treatment and additively manufactured surface on the fatigue behavior of selectively laser melted AISI 316L by using efficient short-time procedures, Int. J. Fatig. 131 (2020), https://doi.org/10.1016/J.IJFATIGUE.2019.105301.
[46] X. Liang, C. Robert, A. Hor, F. Morel, Numerical investigation of the surface and microstructure effects on the high cycle fatigue performance of additive manufactured stainless steel 316L, Int. J. Fatig. 149 (2021) 106273, https://doi.org/10.1016/J.IJFATIGUE.2021.106273.
[47] A. Hamada, M. Jaskari, T. Gundgire, A. Järvenpää, Enhancement and underlying fatigue mechanisms of laser powder bed fusion additive-manufactured 316L stainless steel, Mater. Sci. Eng., A 873 (2023) 145021, https://doi.org/10.1016/J.MSEA.2023.145021.
[48] C. Elangeswaran, A. Cutolo, G.K. Muralidharan, C. de Formanoir, F. Berto, K. Vanmeensel, B. Van Hooreweder, Effect of post-treatments on the fatigue behaviour of 316L stainless steel manufactured by laser powder bed fusion, Int. J. Fatig. 123 (2019) 31–39, https://doi.org/10.1016/J.IJFATIGUE.2019.01.013.
[49] M. Jaskari, A.S. Hamada, T. Gundgire, A. Järvenpää, P. Karjalainen, Effect of isothermal annealing on residual stresses and fatigue properties of LPBF 316L steel, Key Eng. Mater. 964 (2023) 13–18, https://doi.org/10.4028/P-ODGL5N.
[50] D. Hu, J. Pan, J. Mao, S. Hu, X. Liu, Y. Fu, R. Wang, Mechanical behavior prediction of additively manufactured components based on defect evolution observation by synchrotron radiation X-ray tomography, Mater. Des. 198 (2021) 109353, https://doi.org/10.1016/J.MATDES.2020.109353.
[51] K. Wang, H. Jing, L. Xu, L. Zhao, Y. Han, K. Song, X. Qi, M. Su, Fracture mechanism of a Ni-base alloy under high-temperature cyclic deformation: experiments and microstructure characterization, Mater. Char. 189 (2022) 111944, https://doi.org/10.1016/J.MATCHAR.2022.111944.
[52] M. Benedetti, C. Santus, Notch fatigue and crack growth resistance of Ti-6Al-4V ELI additively manufactured via selective laser melting: a critical distance approach to defect sensitivity, Int. J. Fatig. 121 (2019) 281–292, https://doi.org/10.1016/J.IJFATIGUE.2018.12.020.
[53] A. Isaac, F. Sket, W. Reimers, B. Camin, G. Sauthoff, A.R. Pyzalla, In situ 3D quantification of the evolution of creep cavity size, shape, and spatial orientation using synchrotron X-ray tomography, Mater. Sci. Eng., A 478 (2008) 108–118, https://doi.org/10.1016/J.MSEA.2007.05.108.
[54] A. Yadollahi, N. Shamsaei, Additive manufacturing of fatigue resistant materials: challenges and opportunities, Int. J. Fatig. 98 (2017) 14–31, https://doi.org/10.1016/J.IJFATIGUE.2017.01.001.
[55] P.D. Nezhadfar, R. Shrestha, N. Phan, N. Shamsaei, Fatigue behavior of additively manufactured 17-4 PH stainless steel: synergistic effects of surface roughness and heat treatment, Int. J. Fatig. 124 (2019) 188–204, https://doi.org/10.1016/J.IJFATIGUE.2019.02.039.
[56] J. Gockel, L. Sheridan, B. Koerper, B. Whip, The influence of additive manufacturing processing parameters on surface roughness and fatigue life, Int. J. Fatig. 124 (2019) 380–388, https://doi.org/10.1016/J.IJFATIGUE.2019.03.025.
[57] J. Kluczyński, L. Śnieżek, K. Grzelak, J. Torzewski, I. Szachogłuchowicz, M. Wachowski, The influence of process parameters on the low-cycle fatigue properties of 316L steel parts produced by powder bed fusion, Metall Mater Trans

A Phys Metall Mater Sci 54 (2023) 196–210, https://doi.org/10.1007/S11661-022-06858-0/FIGURES/13.
[58] S. Hatami, T. Ma, T. Vuoristo, J. Bertilsson, O. Lyckfeldt, Fatigue strength of 316L stainless steel manufactured by selective laser melting, J. Mater. Eng. Perform. 29 (2020) 3183–3194, https://doi.org/10.1007/S11665-020-04859-X/FIGURES/16.
[59] J.W. Pegues, M.D. Roach, N. Shamsaei, Additive manufacturing of fatigue resistant austenitic stainless steels by understanding process-structure–property relationships, Mater. Res. Lett. 8 (2020) 8–15, https://doi.org/10.1080/21663831.2019.1678202.
[60] F. Fan, M. Jiang, P. Wang, C. Liu, Z. Liu, Z. Chen, Defect-associated microstructure evolution and deformation heterogeneities in additively manufactured 316L stainless steel, Mater. Sci. Eng., A 861 (2022) 144287, https://doi.org/10.1016/J.MSEA.2022.144287.
[61] Y. Murakami, Material defects as the basis of fatigue design, Int. J. Fatig. 41 (2012) 2–10, https://doi.org/10.1016/j.ijfatigue.2011.12.001.
[62] L. Cui, F. Jiang, R.L. Peng, R.T. Mousavian, Z. Yang, J. Moverare, Dependence of microstructures on fatigue performance of polycrystals: a comparative study of conventional and additively manufactured 316L stainless steel, Int. J. Plast. 149 (2022) 103172, https://doi.org/10.1016/J.IJPLAS.2021.103172.
[63] Z. Li, T. Voisin, J.T. McKeown, J. Ye, T. Braun, C. Kamath, W.E. King, Y.M. Wang, Tensile properties, strain rate sensitivity, and activation volume of additively manufactured 316L stainless steels, Int. J. Plast. 120 (2019) 395–410, https://doi.org/10.1016/J.IJPLAS.2019.05.009.
[64] W. Woo, J.S. Jeong, D.K. Kim, C.M. Lee, S.H. Choi, J.Y. Suh, S.Y. Lee, S. Harjo, T. Kawasaki, Stacking fault energy analyses of additively manufactured stainless steel 316L and CrCoNi medium entropy alloy using in situ neutron diffraction, Sci. Rep. 10 (1) (2020) 1–15, https://doi.org/10.1038/s41598-020-58273-3, 10 (2020).
[65] S. Shyamal, M.G. Farahani, T. Allam, A.S. Hamada, C. Haase, J.I. Kömi, P. C. Chakraborti, P. Sahu, Activation of a hybrid twinning mechanism in a Cr-Ni-Si-V-N medium manganese austenitic steel containing precipitates, Scripta Mater. 192 (2021) 83–88, https://doi.org/10.1016/J.SCRIPTAMAT.2020.10.011.
[66] T. Tomaszewski, Modelling of critical defect distributions for estimating the size effect of selective laser melted 316L stainless steel, Int. J. Fatig. 167 (2023) 107378, https://doi.org/10.1016/J.IJFATIGUE.2022.107378.
[67] Y. Fujimoto, W.-B. Kim, E. Shintaku, F. Huang, Applicability of fracture mechanics to very small cracks or the cracks in the early stage, Proc. 2nd Int. Conf. Mech. Behav. Mater. (1998) 627–631, https://doi.org/10.2534/JJASNAOE1968.1998.184_311 (1976).
[68] A. Riemer, S. Leuders, M. Thöne, H.A. Richard, T. Tröster, T. Niendorf, On the fatigue crack growth behavior in 316L stainless steel manufactured by selective laser melting, Eng. Fract. Mech. 120 (2014) 15–25, https://doi.org/10.1016/j.engfracmech.2014.03.008.
[69] O. Fergani, A. Bratli Wold, F. Berto, V. Brotan, M. Bambach, Study of the effect of heat treatment on fatigue crack growth behaviour of 316L stainless steel produced by selective laser melting, Fatig. Fract. Eng. Mater. Struct. 41 (2018) 1102–1119, https://doi.org/10.1111/FFE.12755.